Journal of Colloid and Interface Science 643 (2023) 626–639

Contents lists available at ScienceDirect

Journal of Colloid And Interface Science

journal homepage: www.elsevier.com/locate/jcis

3D space-confined $Co_{0.85}Se$ architecture with effective interfacial stress relaxation as anode material reveals robust and highly loading potassium-ion batteries

Wei-Wen Shen, Yi-Yen Hsieh, Hsing-Yu Tuan *

Department of Chemical Engineering, National Tsing Hua University, Hsinchu 30013, Taiwan

HIGHLIGHTS

- The utilization of 3D nitrogen-doped carbon confined $Co_{0.85}Se$ nanocrystals ($Co_{0.85}Se$@NC) as an anode for potassium ion batteries leads to the achievement of a long cycle life exceeding 4000 cycles.
- $Co_{0.85}Se$@NC anode provide a capacity of 155.6 mA h g^{-1} at 10 A g^{-1}.
- $Co_{0.85}Se$@NC anode shows the areal capacity up to 1.03 mA h cm^{-2} at 500 mA g^{-1}.
- Finite element analysis shows the 3D confinement strategy has the lowest interfacial stress.
- Hundreds of LED bulbs were lighted by a pouch-type potassium-ion full battery composed of $Co_{0.85}Se$@NC anodes.

GRAPHICAL ABSTRACT

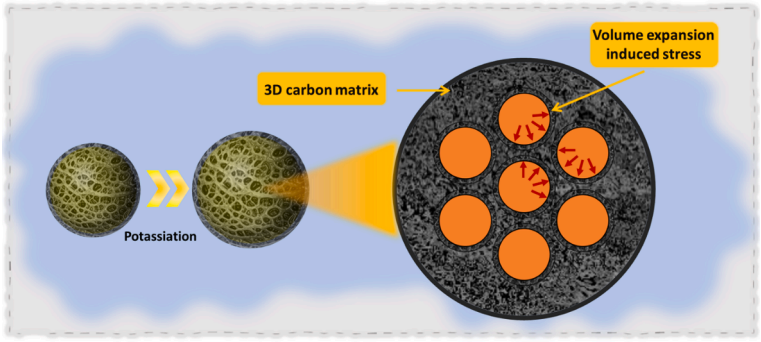

ARTICLE INFO

Keywords:
Potassium ion battery
Metal chalcogenide
Anode
Space-confined
Stress relaxation

ABSTRACT

Conversion-type transition metal chalcogenide anodes could bring relatively high specific capacity in potassium ion storage due to multiple electron transport reactions, but often accompanying huge volume changes and resulting in low cycle life and rapid capacity fading. While electrode materials are closely packed, the contact at the interface during potassiation/depotassiation is similar to point-to-point contact, generating strong stress to make self-aggregation occur. In this work, we constructed a 3D carbon framework to confine $Co_{0.85}Se$ nanocrystals in three-dimensional space, both fulfilling the requirements of the material's size in the nano-scale and providing the largest contact area for releasing stress. With this optimization, nitrogen-doped carbon confined $Co_{0.85}Se$ nanocrystals ($Co_{0.85}Se$@NC) reach an ultra-stable cycle life over 4000 times with a specific capacity of 190.9 mA h g^{-1} at 500 mA g^{-1} and provide 155.6 mA h g^{-1} at 10 A g^{-1} in the rate capability test. It also renders the areal capacity up to 1.03 mA h cm^{-2} at 500 mA g^{-1} in the high-mass loading test. Furthermore, based on the finite element analysis, the 3D confinement strategy has the lowest interfacial stress, ensuring $Co_{0.85}Se$ nanocrystals with high structural integrity. This strategy can relieve the stress issue in the conversion-type anode and demonstrate superior electrochemical performance even at high-loading mass electrodes.

* Corresponding author.
E-mail address: hytuan@che.nthu.edu.tw (H.-Y. Tuan).

https://doi.org/10.1016/j.jcis.2023.04.018
Received 13 February 2023; Received in revised form 21 March 2023; Accepted 4 April 2023
Available online 10 April 2023

1. Introduction

Electrochemical energy storage in batteries is seen as a key component of the future energy economy, automotive and electronics industries. The global installed battery capacity is expected to exceed 1 TWh by 2030 [1]. While the needs of these industries have so far been desirous, the way of replacing fossil energy with energy from renewable sources is further critical for us [2]. Among them, lithium-ion batteries (LIBs) reduce carbon emissions by powering electric vehicles (EVs) and promoting the development of renewable energy through grid-scale energy storage [3]. However, given the limited and uneven geographical distribution of lithium resources in the Earth's crust (0.0017 wt%), the rapid growth of EVs and renewable energy markets has stimulated the pursuit of highly reliable alternatives to commercial LIBs. The highly cost of lithium makes scientists search for other battery system composed of earth-abundant elements [4]. Since the rechargeable potassium-ion batteries (PIBs) was first invented by Eftekhari in 2004 [5], and stands out by its significant advantages: (a) high abundance (2.09 wt% in the crust) and low cost [6]; (b) lower standard redox potential (−2.93 V for K^+/K), which guarantees a higher operating voltage and higher energy density for the batteries; (c) faster ion diffusion kinetics and lower ion desolvation energy from their weaker Lewis acidity [7]. Hence, the K ions have the highest ion conductivity in organic electrolytes among these three alkali ions (Li^+, Na^+, and K^+) [8]; (d) there is no alloy reaction with potassium while using aluminum foil as the current collector, replacing the more expensive copper foil in LIBs [9].

Due to the high theoretical specific capacities and unique structural features, metal chalcogenides have been seen as potential anode materials for PIBs [10,11]. Among which ferromagnetic metal (Fe, Co, and Ni) sulfides and selenides are denoted as MXs, M = Fe, Co, Ni; X = S, Se) show strong competitiveness by their excellent advantages [12–14]. First, these three metals are relatively abundant in the earth's crust, while large amounts of MXs are stably present in some natural ores. Second, the electrochemical performances can be improved by the morphological controllability of MXs. Third, benefiting from a single transformation-type reaction mechanism, MXs can both provide high specific capacity and demonstrate excellent cycle life. Fourth, compared with ferromagnetic metal oxides, ferromagnetic metal sulfides and selenides have better reaction kinetics in the conversion reaction because the M−S/Se bond is weaker than the M−O band, and with higher electrical conductivity than that of ferromagnetic metal oxides. As for the ferromagnetic metal telluride, the rarity of tellurium greatly limits its cost competitiveness [15]. In general, the K^+ storage of MXs can be described as a multi-step reaction during discharge. The intercalation reaction occurs at a relatively high potential ($MX + yK^+ + ye^- \rightarrow K_yMX$), during which the structural integrity can be maintained with small volume change. Thereafter, the conversion reaction occurs in a deeper discharge state ($K_yMX + zK^+ + ze^- \rightarrow M + K_y + zX$), accompanied by phase transition and large volume expansion.

The huge volume expansion (about 312%) and consequent uneven stress distribution lead to structural cracking, making both ionic and electronic conduction paths to be disrupted in the electrodes. The combination with conductive carbon is an effective strategy to modify this drawback [16]. Carbonaceous materials exhibit fascinating properties, including high electrical conductivity, large surface area, and excellent mechanical strength [17]. In carbon-MXs composites, carbon acts as a matrix to buffer volume changes and prevent self-aggregation of MXs, which is beneficial for long-term cycling stability [18,19]. So far, several progresses have been made in designing MXs composites with various carbonaceous materials [20]. For example, CoS_2 has been successfully anchored to the surface of carbon nanotubes [21]; however, after a long-term cycling process, the aggregation and structural crushing are still unavoidable. Structures with several customized morphologies were proposed. For example, the 1D-CNT $FePSe_3$ composite can provide stable cycling life for over 1000 times and maintain a specific capacity of 223.6 mA h g^{-1} [22]. Compared with the former, mixing MXs with carbonaceous materials [23,24], such as graphene oxide and carbon nanotube network is another promising strategy for reaching high-quality anode materials [25,26]. Graphene significantly improves the electrical conductivity and charge transfer of pure MXs. At the same time, MXs can alleviate graphene restacking to maintain a large surface area [27]. However, when the nanocrystals were anchored to graphene to provide a fairly good stress buffer, the contact between the nanoparticle and the adjacent nanoparticle still cannot be prevented, crushing the particles by a large stress gradient in these contacts after long-term cycling.

Self-aggregation and direct contact of nanoparticles are key issues for K ion storage [28], where point-to-point contacts result in a large stress gradient [29]. To avoid these problems, we propose a stress management strategy by encapsulating nanocrystals in a 3D nitrogen-doped carbon (NC) framework to increase the contact area. $Co_{0.85}Se$@NC composites were formed by a 3D carbon framework and cobalt selenide nanocrystals, in which the metal selenide nanocrystals with size in nanoscale and were evenly separated by the carbon framework, inhibiting the self-aggregation and providing a more uniform stress distribution. The three-dimensional carbon framework fully separated the nanocrystals, providing the largest contact area to reduce the stress. Finite element analysis (FEA) was also carried out to predict stress distribution, proving that the 3D structure has the lowest stress among the three models. In the view of the macroscale, the $Co_{0.85}Se$@NC has almost no cracks on the electrode surface, whereas $Co_{0.85}Se$ nanocrystals were in the opposite situation. For the electrochemical performances, $Co_{0.85}Se$@NC can provide a long-life span for over 4000 cycles with 190.9 mA h g^{-1} at 500 mA g^{-1}. The importance of stress management was further verified with high-loading mass half-cell tests. As the loading exceeds 2.4 mg cm^{-2}, the whole performances were dominated by the stress problem. Further, we successfully made the loading mass to 4.61 mg cm^{-2} with a high areal capacity of 1.03 mA h cm^{-2}. In short, we provide an effective way to enhance the performance of conversion-type anode in PIBs.

2. Results and discussion

We establishe three models to predict the stress distribution of cobalt selenide nanocrystals at different configurations, (1) nanocrystals closely packed (Fig. 1a), (2) 2D graphene oxide (GO) composite (Fig. 1b) and (3) 3D amorphous carbon composite (Fig. 1c). The expansion behavior of potassiation was replaced by the thermal expansion, and the corresponding volume change was calculated in Table. S1. Here, the mechanical properties of cobalt selenide nanocrystals, monolayer graphene oxide, and amorphous carbon are showed in Table. S2. The coefficient of thermal expansion cobalt selenide nanocrystals is at a constant value. When the nanocrystals are tightly packed, there is nowhere to release the stress but to damage the interface, leaving lots of crystal fragments. The new interface will consume potassium ions to form a new SEI layer, which is lined with the following cycling test that the cobalt selenide nanocrystals would have a sharp increase in capacity. Meanwhile, SEI layer generation reduces the number of active materials, corresponding to the short cycle life. With the introduction of graphene oxide (Fig. 1b), the stress between them can be released through the flat two-dimensional structure. Limited by the 2D structure, the nanocrystals on the same layer of GO are not completely separated, where point-to-point contact will be the same as the above packed nanocrystals. Owing to the strong mechanical properties, the overall structural stability can still be maintained. However, broken fragments of cobalt selenides passed through the GO to dissolve into the electrolyte, corresponding to the instability of $Co_{0.85}Se$@GO after long-term cycling. The amorphous carbon acts as a stress regulator by providing sufficient contact area to minimize the interfacial stress (Fig. 1c). The expansion of nanoparticles leads to relatively huge stresses on the amorphous carbon near the interface. The accumulated stress can be isotropically released

by the spherical structure. In Fig. 1d, the slope rose sharply in $Co_{0.85}Se$ nanocrystals when the degree of expansion was about 0.64, meaning that the nanocrystals can't bear such a large stress but lead to cracking. The stress is reduced for the 2D confinement strategy, and the top-side contact of nanocrystal-graphene oxide is much smaller than the side-side by the superior mechanical properties of GO. The side-side contact is almost the same as stacked nanocrystals, theie slope increases gradually as the degree of expansion exceeded 0.4. As for the 3D confinement strategy, the stress is released and the overall structural integrity can be maintained. The slope doesn't increase evidently, which means the structure can significantly bear the expansion. Fig. 1e shows the maximum stress value in each model when the expansion degree is 1.0.

Fig. 2a shows the synthesis schematic diagram of $Co_{0.85}Se$@NC microspheres. Co DH-glycerol composites were synthesized via the solvothermal method with cobalt nitrate hexahydrate as the cobalt source, glycerol, and isopropanol as solvents. When the temperature reaches 180 °C, isopropanol and NO^{3-} undergo a redox reaction as the following formula: $4(CH_3)_2CHOH + NO^{3-} \rightarrow 4CH_3\ COCH_3 + NH_3 + OH^- + 2H_2O$. The released hydroxide ions precipitate Co^{2+} to form Co double hydroxide (Co DH). Meanwhile, glycerol molecules self-assemble into a quasi-emulsion in isopropanol through strong intermolecular hydrogen bonds under solvothermal conditions, serving as a soft template for Co DH growth [30]. Then, a sol–gel application process covered the surface of the Co DH-glycerol composite with dopamine (PDA). This component molecule mimics adhesion proteins because it contains catechol and amine functional groups. At weak alkaline pH, dopamine is easily oxidized by dissolved oxygen to form dopamine quinone, followed by a sequence of cyclized, oxidized, rearranged, and self-polymerized into PDA [31]. To obtain $Co_{0.85}Se$@NC composites, the as-synthesized Co DH-glycerol composite was subjected to one-step annealing and selenization under Ar/H_2 atmosphere. Scanning electron microscope (SEM) image shows that the $Co_{0.85}Se$@NC composite has a three-dimensional spherical structure with an average diameter of 900 nm (Fig. 2b, c). The $Co_{0.85}Se$ nanoparticles are uniformly embedded in the carbon spheres with PDA (50 nm) covering the outside. The $Co_{0.85}Se$ nanoparticles (about 70 nm) through transmission electron microscopy (TEM) (Fig. 2d) are uniformly spaced. The three-dimensional carbon

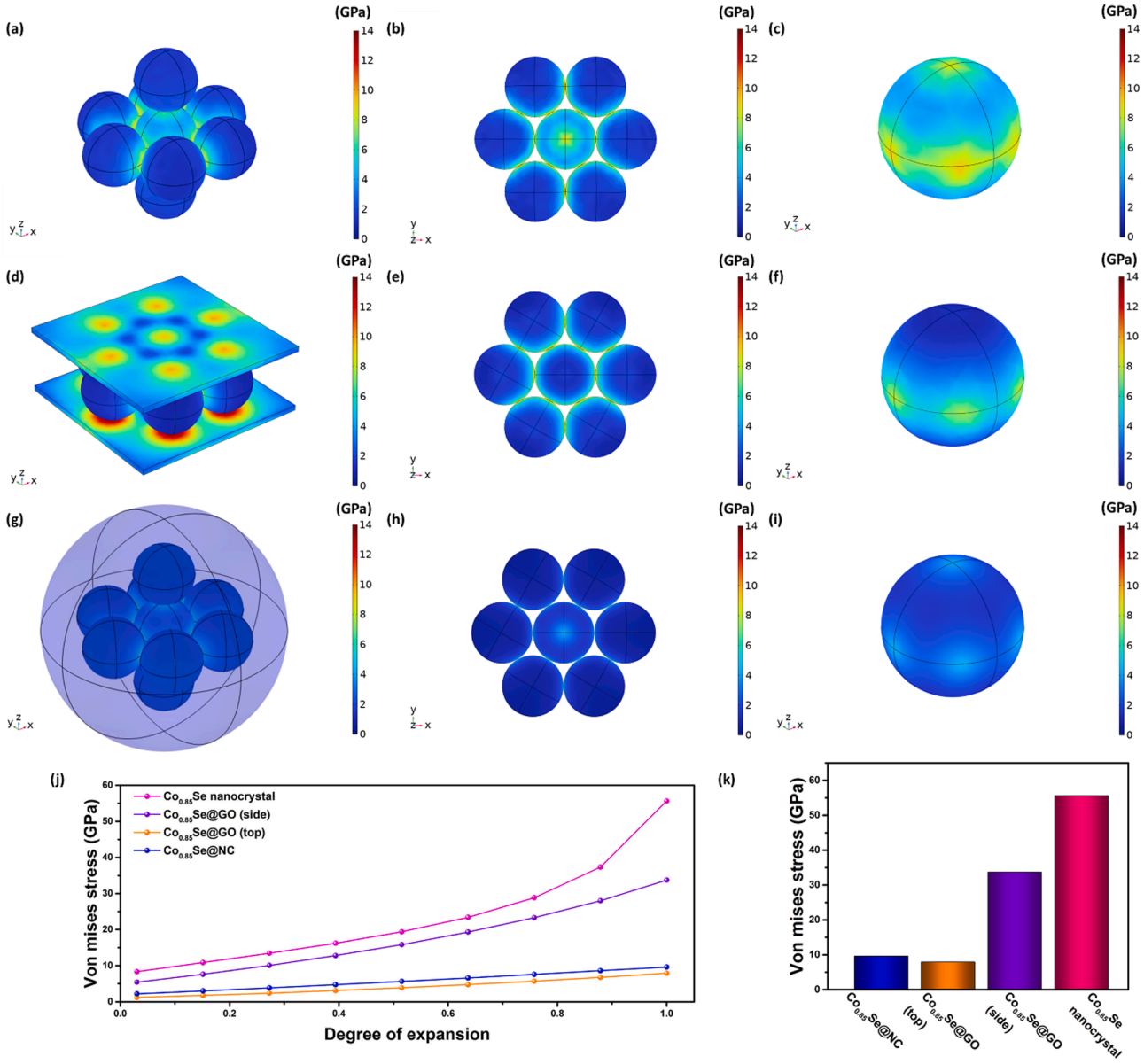

Fig. 1. Finite elemental analysis. The modeled stress distribution of (a-c) $Co_{0.85}Se$ nanocrystals, (d-f) $Co_{0.85}Se$@GO, and (g-i) $Co_{0.85}Se$@NC in 3D-view, 2D-view, and single nanocrystal. (j) The corresponding stress value at different degrees of expansion and (k) the value after full expansion.

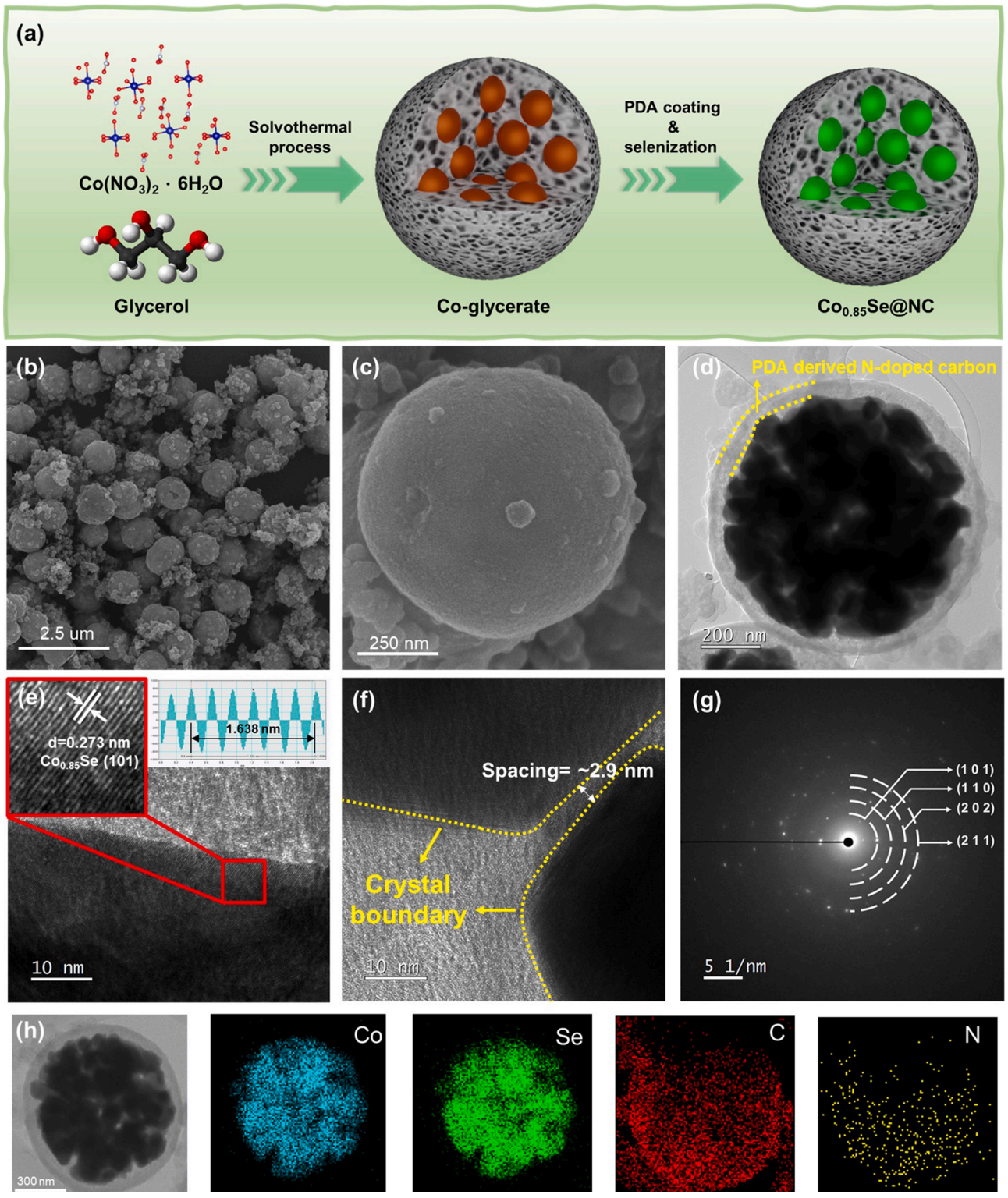

Fig. 2. Material characterization of $Co_{0.85}Se$@NC. (a) schematic illustration of synthesis process of $Co_{0.85}Se$@NC. (b, c) SEM images. (d) TEM images. (e, f) high resolution TEM images. (g) SAED pattern. (h)EDS element mapping.

sphere structure can both prevent the self-aggregation of nanoparticles and buffer the volume expansion during the potassiation/depotassiation process. (Fig. 2f). Fig. 2e clearly shows that the lattice fringes of $Co_{0.85}Se$@NC with a d-spacing of 0.273 nm were matched well with the (1 0 1) plane of $Co_{0.85}Se$. Selected area electron diffraction (SAED) shows four annular patterns corresponding to the (1 0 1), (1 1 0), (2 0 2), and (2 1 1) crystal planes (Fig. 2g), which were consistent with the diffraction peaks of the X-ray diffraction (XRD) results (the hexagonal crystal structure of $Co_{0.85}Se$ PDF 04–006-8806) [32]. Furthermore, energy dispersive spectroscopy (EDS) analysis results (Fig. 2h) indicates that $Co_{0.85}Se$@NC contains Co, Se, C, and N elements. The corresponding EDS mapping images show that they are uniformly distributed, where the N element is from the outer layer of PDA after annealing. We synthesized $Co_{0.85}Se$ nanocrystal, graphene oxide confined $Co_{0.85}Se$

($Co_{0.85}Se$@GO), and $Co_{0.85}Se$@NC, the corresponding XRD patterns are showed in Fig. S1a. All the diffraction peaks correspond to the $Co_{0.85}Se$ phase of the hexagonal crystal structure (*P*63/*mmc* (194), PDF 04–006-8806). From the Raman spectrum in Fig. S1b, the intensity of the D band near 1350 cm^{-1} (corresponding to disordered or defective carbon) is similar to the G band near 1580 cm^{-1} (corresponding to graphitic carbon). The relative intensity ratio ($I_D/I_G = 0.978$) can reflect the number of structural defects and the degree of graphitization, improving the electrical conductivity and the reaction kinetics [33,34]. The result investigated by N_2 adsorption/desorption tests (Fig. S1c, d) shows that $Co_{0.85}Se$@NC has a typical type IV curve with a high specific surface area (137.8 $m^2\ g^{-1}$) and mesoporous structure (4.9 nm).[35] Accordingly, the 3D network and the porous structure can improve electrons and ions transportation, playing an essential role in storing potassium ions in PIBs. The thermogravimetric analysis (TGA) curve is shown in the Fig. S1e, the accurate carbon content can be calculated as 21.61% (Fig. S5). The composition and chemical state of $Co_{0.85}Se$@NC were determined by X-ray photoelectron spectroscopy (XPS) as shown in Fig. S1f–i. The Co 2p high-resolution spectrum can be resolved into six fitted peaks (Fig. S1f). Specifically, the prominent peaks observed at 778.4 and 793.0 eV are assigned to Co $2p_{3/2}$ and Co $2p_{1/2}$ of Co^{3+}, while those at 781.5 and 796.8 eV are assigned to Co $2p_{3/2}$ and Co $2p_{1/2}$ of Co^{2+}. There are two satellite peaks at 786.9 and 801.0 eV originating from the excitation of the remaining bound electrons, indicating the existence of mixed oxidation states in $Co_{0.85}Se$@NC [36]. In the case of the Se 3d spectrum (Fig. S1g), peaks of Se $3d_{5/2}$ and Se $3d_{3/2}$ of Se^{2-} at 54.3 and 56.2 eV, while the other two fitted peaks at 63.1 and 59.2 eV are related to Co $3p_{3/2}$ and Se-O bonds originating from the Co-Se bonds and the partial oxidation of Se on the surface. For the N 1 s spectrum (Fig. S1h), there are four types of N species, pyridine N at 398.4 eV, pyrrolic N at 399.5 eV, graphitic N at 400.7 eV and oxide N at 403.7 eV. N-doped carbon has higher adsorption energy for K_2Se to reduce the dissolution of it from carbon matrix pores during cycling [37]. The C 1 s peaks correspond to sp^2 C—C, sp^3 C—C, and C═O at 284.8, 285.9, and 288.2 eV, respectively, where C═O is originated from the partial oxidation of the material exposed to air, as shown in Fig. S1i.

The electrochemical performance of $Co_{0.85}Se$@NC was evaluated by assembling coin-type half cells. Fig. 3a shows the cyclic voltammetry (CV) curves of $Co_{0.85}Se$@NC in the first four cycles at a scan rate of 0.1 mV s^{-1}. For the first cathodic scan, the reduction peak at 0.65 V is attributed to the SEI formation at the electrode–electrolyte interface during the initial potassiation. The peak at 0.41 V belongs to the conversion reaction of $K_xCo_{0.85}Se$ to Co and K_2Se. Subsequently, the K^+ intercalation reaction in carbon is around 0.01 V. Conversely, in the anodic scan, the oxidation peak at 0.47 V corresponding to the deintercalation of K^+ from carbon. The following two peaks at 1.65 V and 2.2 V belong to Co and K_2Se to generate $K_xCo_{0.85}Se$ and further generate $Co_{0.85}Se$, respectively. Starting from the third cycle, the curves are completely overlapped, implying its superior reversibility of $Co_{0.85}Se$@NC. From the in-situ XRD patterns (Fig. S6) during the first discharge process, the peak intensity decreases at about 20° and 32.9° are caused by the formation of low crystallinity K_2Se (PDF 00–023-

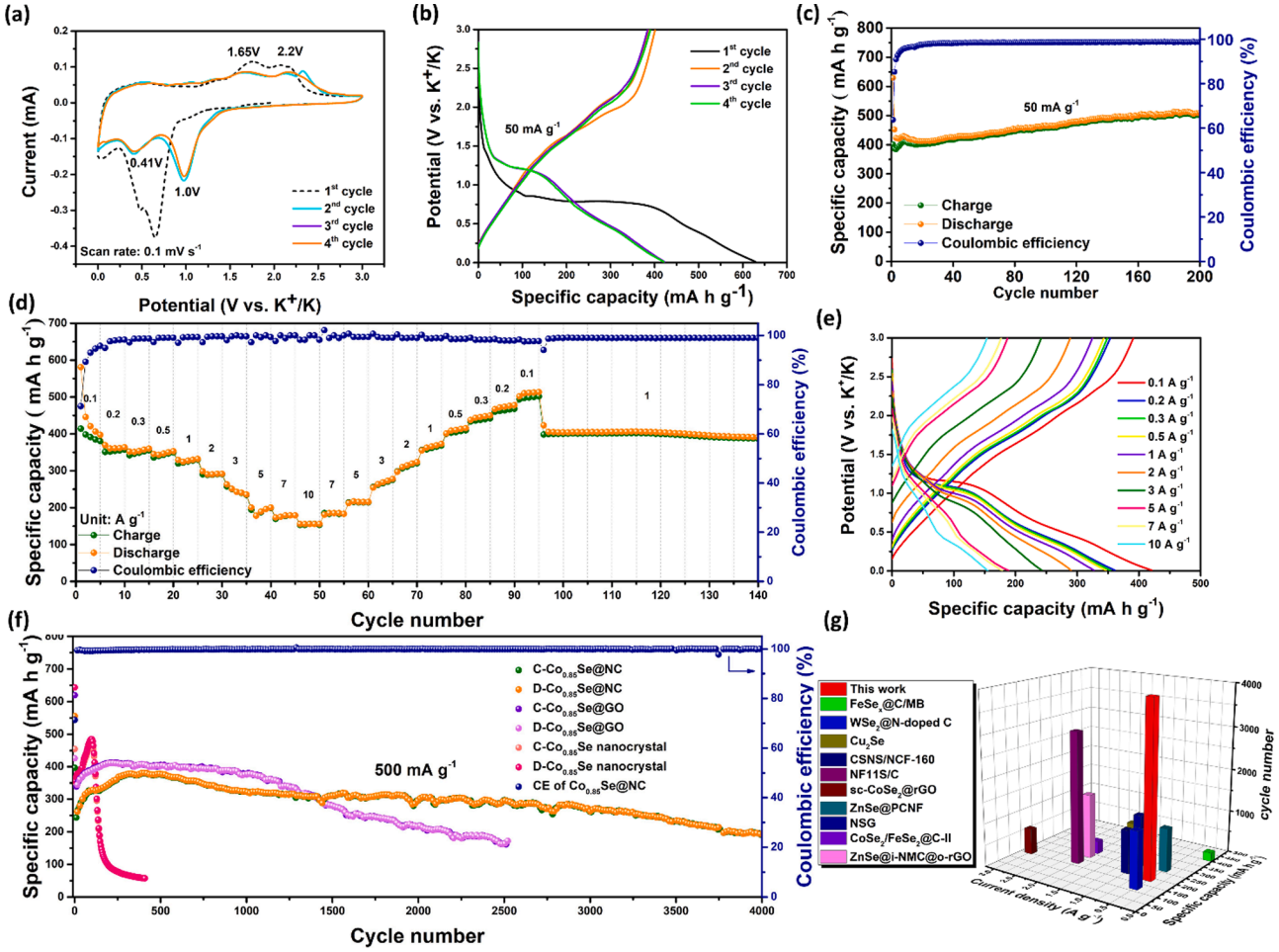

Fig. 3. (a) CV profile of $Co_{0.85}Se$@NC electrode. (b) charge/discharge curve of $Co_{0.85}Se$@NC electrode at 50 mA g^{-1}. (c) charge/discharge curve of $Co_{0.85}Se$@NC electrode in different cycle. (d) rate performance of $Co_{0.85}Se$@NC. (e) charge/discharge curve of $Co_{0.85}Se$@NC at various current density. (f) Long-term cycling stability of $Co_{0.85}Se$ nanocrystal, $Co_{0.85}Se$@GO and $Co_{0.85}Se$@NC. (g) Electrochemical performances comparison in the field of selenium-based materials.

0470). In addition, the peak at 33.5° corresponds to the (1 0 1) plane of the $Co_{0.85}Se$ phase and is slightly shifts to a smaller angle at the first discharge state due to the insertion of K^+. Also, the reaction is reversible by observing the peak again after charging to 3 V. The ex-situ XPS revealed that both Co 2p and Se 3d shift to lower binding energy through the reduction of Co and formation of the K-Se bonding after discharge to 0.01 V. After charging to 3 V, they shift to high binding energy and gradually return to their original positions [38,39]. The ex-situ TEM image further confirms the products after completely potassiated are Co and K_2Se (Fig. S7). Fig. 3b shows the galvanostatic charge–discharge (GCD) curves of $Co_{0.85}Se$@NC for the first four cycles, the initial discharge/charge capacities of 583.2 and 432.1 mA h g^{-1}, respectively, with an initial Coulombic efficiency of 74.1%.

By examining the GCD curves at the 500, 1000, 1500, 2000, 2500, and 3000th cycle (Fig. S9), respectively, the charge–discharge plateau does not disappear after long-term cycling, indicating that $Co_{0.85}Se$@NC can effectively suppress the shuttle effect of K_2Se [40]. The rate performance of $Co_{0.85}Se$@NC is shown in Fig. 3d, e, its average discharge capacity at current densities of 0.1, 0.2, 0.3, 0.5, 1, 2, 3, 5, 7, and 10 A g^{-1} are 420.7, 353.7, 349.1, 343.3, 325.1, 289.0, 242.6, 187.5, 177.0, and 155.6 mA h g^{-1}, respectively. The outstanding rate performance stems partly from the unique 3D carbon framework of the $Co_{0.85}Se$@NC composite. The porous carbon matrix with large interior space provides fast transport channels for both electrons and ions [41], while $Co_{0.85}Se$ in the form of smaller nanoparticles can shorten electron/ion diffusion path to facilitate charge transfer and rapid pseudocapacitive reactions [42]. When the current density is back to 1 A g^{-1}, the average discharge capacity can still maintain at 400 mA h g^{-1}. Fig. 3f shows the long-term cycling profile of $Co_{0.85}Se$ nanocrystals, $Co_{0.85}Se$@GO and $Co_{0.85}Se$@NC at a current density of 0.5 A g^{-1}. The $Co_{0.85}Se$@NC anode has the best performances by delivering 190.9 mA h g^{-1} after 4000 cycles with a capacity retention of 78.3%. The capacity loss per cycle was 0.014%, confirming its impressive durability. Benefitting from the stress management of the three-dimensional carbon framework, $Co_{0.85}Se$@NC has the advantage of long cycling performance in the field of selenium-based anodes in PIBs as shown in Fig. 3g [37,43–51]. For the application of 3D confinement strategy in PIBs, the $Co_{0.85}Se$@NC has the advantage of long-term cycling performance as shown in Table. S4.

$Co_{0.85}Se$@NC exhibited excellent K^+ storage capability and long-term cycling stability is associated with high-rate pseudocapacitive behavior. To verify the related charge storage mechanism and the kinetics process in the PIB system, we measured and calculated the

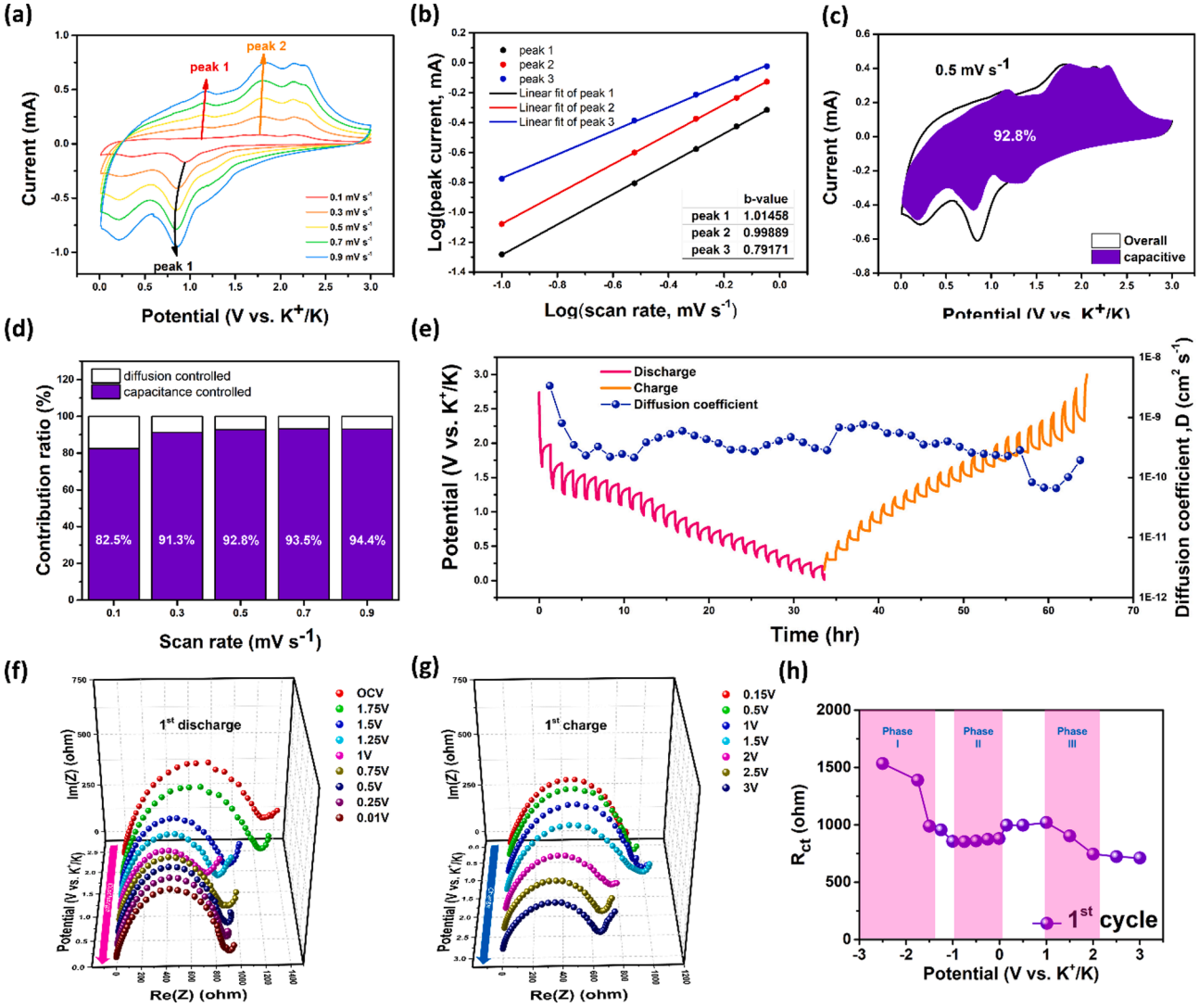

Fig. 4. Kinetic performance and potassium ion diffusion experiment of $Co_{0.85}Se$@NC. (a) CV curves at various scan rates. (b) Linear fitting profiles of log (i, peak current) vs log (v, scan rate). (d) The integral area of $Co_{0.85}Se$@NC displaying the potassium ion diffusion-controlled contribution at 0.5 mV s^{-1}. (d) Capacitance contribution of $Co_{0.85}Se$@NC. (e) GITT profiles and the diffusion coefficient calculated from the obtained GITT results. (f-h) In-situ EIS at first cycle and the corresponding charge transfer resistance profiles.

pseudocapacitive contribution by cyclic voltammetry (CV) at different scan rates (0.1–0.9 mV s^{-1}). Fig. 4a shows the analysis of the capacitive effect of $Co_{0.85}Se$@NC at various scan rates based on CV curves. As expected, the scan rate increases with shape similarity, suggesting that $Co_{0.85}Se$@NC has a stable electrochemical reaction [52]. From the power-law relationship, the relationship between peak current (i) and scan rate (v) can be described as $i = av^b$, where a and b are constants. The "b" value indicates the extent of the capacitive effect: a b value of 0.5 indicates an extreme diffusion-controlled process and an extreme capacitance-controlled process is indicated by a b value of 1.0. By plotting log(i) and log(*v*), the b value can be calculated from the slope after linear fitting [53]. Peaks 1 to 3 have b-values of 1.01, 0.99, and 0.79, respectively. (Fig. 4b). The capacitive contribution can be further quantified using Eq. (1) [54].

$$i(v) = k_1 v + k_2 v^{\frac{1}{2}} \quad (1)$$

where k_1 and k_2 are constant values corresponding to capacitance-controlled and diffusion-controlled processes, respectively [55]. As shown in Fig. 4c, the capacitance ratio during total storage was 92.8% at 0.5 mV s^{-1}. Fig. 4d shows the contribution of the pseudocapacitive behavior at different scan rates. The capacitance ratios are 82.5%, 91.3%, 92.8%, 93.5% and 94.4% at scan rates of 0.1, 0.3, 0.5, 0.7 and 0.9 mV s^{-1}, respectively. At a lower scan rate of 0.5 mV s^{-1}, the

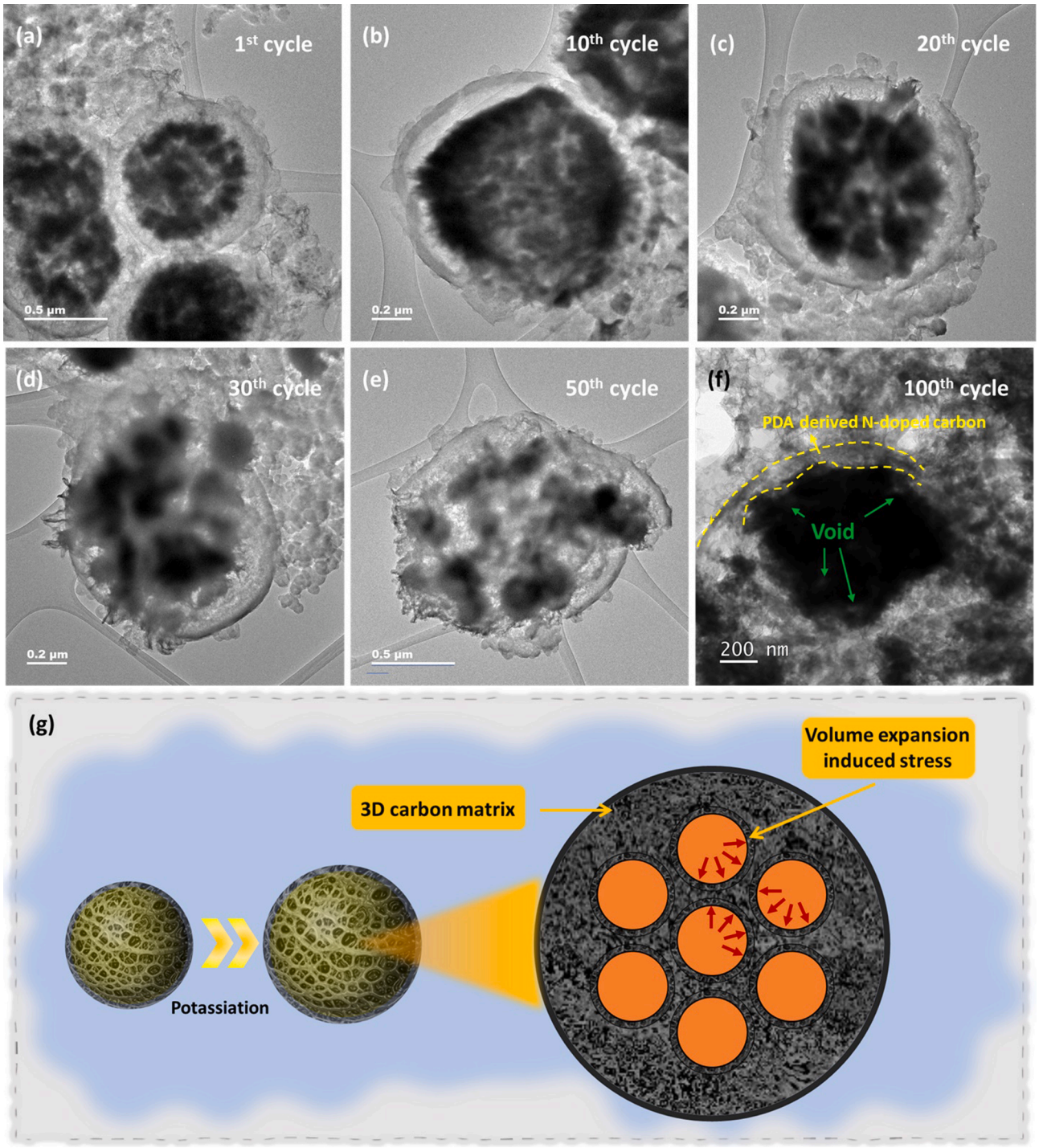

Fig. 5. TEM images after (a) 1st, (b) 10th, (c) 20th, (d) 30th, (e) 50th and (f) 100th cycle. (g) schematic illustration of 3D carbon matrix in stress relaxation.

capacitive contribution still reaches 92.8%, suggesting that pseudocapacitance stores a higher proportion of the total capacity. The reason for the high capacitive contribution may come from the relatively high specific surface area and plentiful interfaces among $Co_{0.85}Se$ nanoparticles [56]. Next, the diffusion coefficient of K^+ in $Co_{0.85}Se$@NC was assessed using the galvanostatic intermittent titration technique (GITT) by applying a series of pulsed currents at 0.1 A g^{-1} for 0.33 h with a rest interval of 0.67 h. The assembled cell was discharged/charged at 0.05 mA g^{-1} for three cycles before GITT measurements. According to Fick's second law, D_{K+} can be calculated by Eq. (2) (Fig. 4e) [57,58].

$$D_{k+} = \frac{4}{\pi\tau}\left(\frac{m_B V_M}{M_B S}\right)^2 \left(\frac{\Delta E_S}{\Delta E_\tau}\right)^2 \quad (2)$$

where m_B, M_B and V_M are the mass, molar mass, and molar volume of the electrode material, respectively, τ is the relaxation time, S is the area of the electrode, ΔE_τ and ΔE_s are the voltage changes in the constant current phase after each equilibration process, L is the thickness of the electrode (Fig. S12). The diffusion coefficients range from 3.36×10^{-9} to 2.84×10^{-10} and 6.80×10^{-10} to 1.94×10^{-10} during potassiation and depotassiation. The Nyquist plots of each potential are shown in Fig. 4f-g by discharging from the open circuit voltage to 0.01 V and then charging to 3 V through in-situ EIS. In Phase I (Fig. 4h), the adsorbed state of K ions begins to intercalate to form $K_xCo_{0.85}Se$, reducing the interface charge transfer resistance. During phase II, increased R_{ct} is due to the volume expansion and formation of the SEI layer, which exhibits resistive properties [59]. As for phase III, the deintercalation of K_2Se and Co reduces the interface transfer resistance.

In the ion storage system, intercalation reactions usually have lower capacity, whereas conversion and alloy reactions offer higher ones. However, during the conversion process, the cleavage and formation of chemical bonds lead to structural collapse and the alloying process results in huge volume changes caused by the formation of binary alloys, providing poor cycle life. Particularly, the $Co_{0.85}Se$ nanocrystal has two main shortcomings. First, a large volume change of 312% after fully potassiated leads to structural collapse. Second, the nanocrystals gradually coarsened into larger particles or aggregated during cycling due to thermally-induced recrystallization and surface energy minimization [60]. In conclusion, the smaller particle size can effectively reduce structural damage and the three-dimensional carbon framework can prevent them from aggregation. Fig. 5a shows the TEM image after the first cycle, the structure remains the same with the diameter of the microspheres at 920 nm. For those at the 10^{th} cycle (Fig. 5b), nanoparticles tend to stay near the surface due to the concentration gradient of K ions. After 20 cycles (Fig. 5c), repeating K^+ insertion/de-insertion makes nanocrystals form larger crystals (about 150 nm). Further, some nanocrystals are filamentous and protrud outward on the surface of the carbon shell, such growth is probably through some fissures during the cycling process. Therefore, the nanocrystals have the chance to contact the diffused K ions directly to form filaments. After 30 cycles (Fig. 5d), more filamentous $Co_{0.85}Se$ penetrate these cracks. Inevitably, the structure inside the microspheres begins to be stretched due to the repeating potassation/depotassiation. The nanocrystals gradually form larger particles in a manner that minimizes the surface energy. After reaching 50 cycles (Fig. 5e), the nanocrystals maintain a size of about 130 nm. In comparison with those at the 20^{th} and 30^{th} cycles, the three-dimensional confinement strategy can keep the nanoparticles' size close to the nano-scale. Although aggregation occurs (Fig. 5f), the overall shape of the microspheres is still maintained, showing the management strategy can effectively alleviate the structural damage. Overall, the introduction of a three-dimensional carbon framework provides an outstanding buffer structure to regulate the stress generated by the potassiation (Fig. 5g).

Metal selenides (MSe_x) is a promising potential from their multiple redox storage mechanisms in PIBs. However, severe volume expansion obviously limited its performance. To tackle this bottleneck, they often compounded with other materials, including various MSe_x, metal oxides, carbonaceous and graphitic materials, etc. [17]. After the introduction of carbonaceous and graphitic materials, the conductivity can be improved. Furthermore, benefiting from the structure robustness, the aggregation and volume expansion can be alleviated for battery application [12]. To check the stress management more clearly, we observed the electrode surface of $Co_{0.85}Se$ nanocrystals, $Co_{0.85}Se$@GO, and $Co_{0.85}Se$@NC at 10^{th} (Fig. 6a, e, i), 50^{th} (Fig. 6b, f, j), and 100^{th} (Fig. 6c, g, k) cycle via SEM. From the electrode surface after 10 cycles (Fig. 6a, b, c), cracks appear on the electrode surface of $Co_{0.85}Se$ nanocrystals, which are getting bigger with increasing cycle numbers. On the basis of stress management, they become smaller after the introduction of GO, and the 2D structure with robust mechanical properties can effectively release the expansion (Fig. 6e, f, g). Moreover, there are no cracks through the 3D carbon matrix management, indicating that we perfectly minimize the stress gradient and kept the electrode structure integrity (Fig. 6i, j, k). The bumps on the surface in Fig. 6j are due to the detachment of the binder during the sample processing.

In the micro-level perspective, the nanocrystals are closely arranged with each other and squeeze outward during cycling. The contacts among them are like point-to-point contact, leading to a large stress gradient at the interface. Eventually, an irreversible loss in specific capacity is caused by the break and dissolution of nanocrystals into the electrolyte. Despite the intervention of the 2D carbon network, larger cracks still appear on the electrode surface with increasing number of cycles, indicating a failure of stress distribution management. The two-dimensional GO can disperse the stress in the longitudinal direction, whereas the 2D structure cannot prevent contacts in the lateral direction, similar to that of the $Co_{0.85}Se$ nanocrystals. Benefiting from the 3D carbon matrix generated from Co DH-glycerol composites, minimizing the stress by providing sufficient contact area. Furthermore, we inspected the electrode cross-sections at the 100^{th} cycle, and the electrode thickness of the $Co_{0.85}Se$ nanocrystals is 32.2 μm (Fig. 6d). With the stress management, the introduction of graphene oxide reduces the thickness by 11.3 μm (Fig. 6h). Especially, the thickness of $Co_{0.85}Se$@NC is further down to 13.2 μm, which is almost one-third of the nanocrystals.

We conducted cycling performance tests of $Co_{0.85}Se$@NC, $Co_{0.85}Se$@GO and $Co_{0.85}Se$ nanocrystals at different loading mass to reveal the importance of stress management. While the loading mass of the $Co_{0.85}Se$@NC up to 4.25 mg cm^{-2}, its specific capacity only decreased from 411.7 mA h g^{-1} to 333.9 mA h g^{-1} at 50 mA g^{-1}, with capacity retention maintained at 81.1% (Fig. 7a). As the mass loading of the $Co_{0.85}Se$@GO and $Co_{0.85}Se$ nanocrystal reach 3.65 and 4.17 mg cm^{-2}, their specific capacity at the 10^{th} cycle is dropped to 318.47 and 173.69 mA h g^{-1} at 50 mA g^{-1}, respectively. Further, those at the 50^{th} cycle rapidly drop to 227.43 and 12.34 mA h g^{-1}, respectively. Interestingly, $Co_{0.85}Se$@NC, $Co_{0.85}Se$@GO, and $Co_{0.85}Se$ nanocrystals are all maintained normal cycling performance for the loading mass less than 2.4 mg cm^{-2}. As the loading mass exceeds this range, stress become the main role in affecting the cycle performance. Such a rapid capacity decay is attributed to the server volume expansion at high loading. The pulverization of the internal structure leads to an increase in the ohmic overpotential and irreversible reaction. On the other hand, we also tested its rate capability for different loading masses (1.75, 2.35, and 3.75 mg cm^{-2}). The specific capacity is decreased with increasing loading mass at various current densities. Through Fig. 7d, the average discharge capacity of $Co_{0.85}Se$@NC (3.75 mg cm^{-2}) are 373.11, 296.56, 248.07, 175.75, and 142.81 mA h g^{-1} at current densities of 100, 500, 1000, 2000, and 2500 mA g^{-1}, respectively. The capacity retention (relative to 1.75 mg cm^{-2}) is 95.2, 85.6, 78.7, 72.0, and 66.9%, respectively (Fig. 7g). For that of $Co_{0.85}Se$@GO (3.75 mg cm^{-2}) is 322.99, 227.05, 174.44, 103.70, and 60.64 mA h g^{-1}, respectively (Fig. 7e). The capacity retention (relative to 1.75 mg cm^{-2}) of 87.3, 86.0, 75.1, 59.1, and 43.4%, respectively (Fig. 7h). The $Co_{0.85}Se$ nanocrystals (3.75 mg cm^{-2}) only provide capacities of 175.22, 84.79, 43.98,

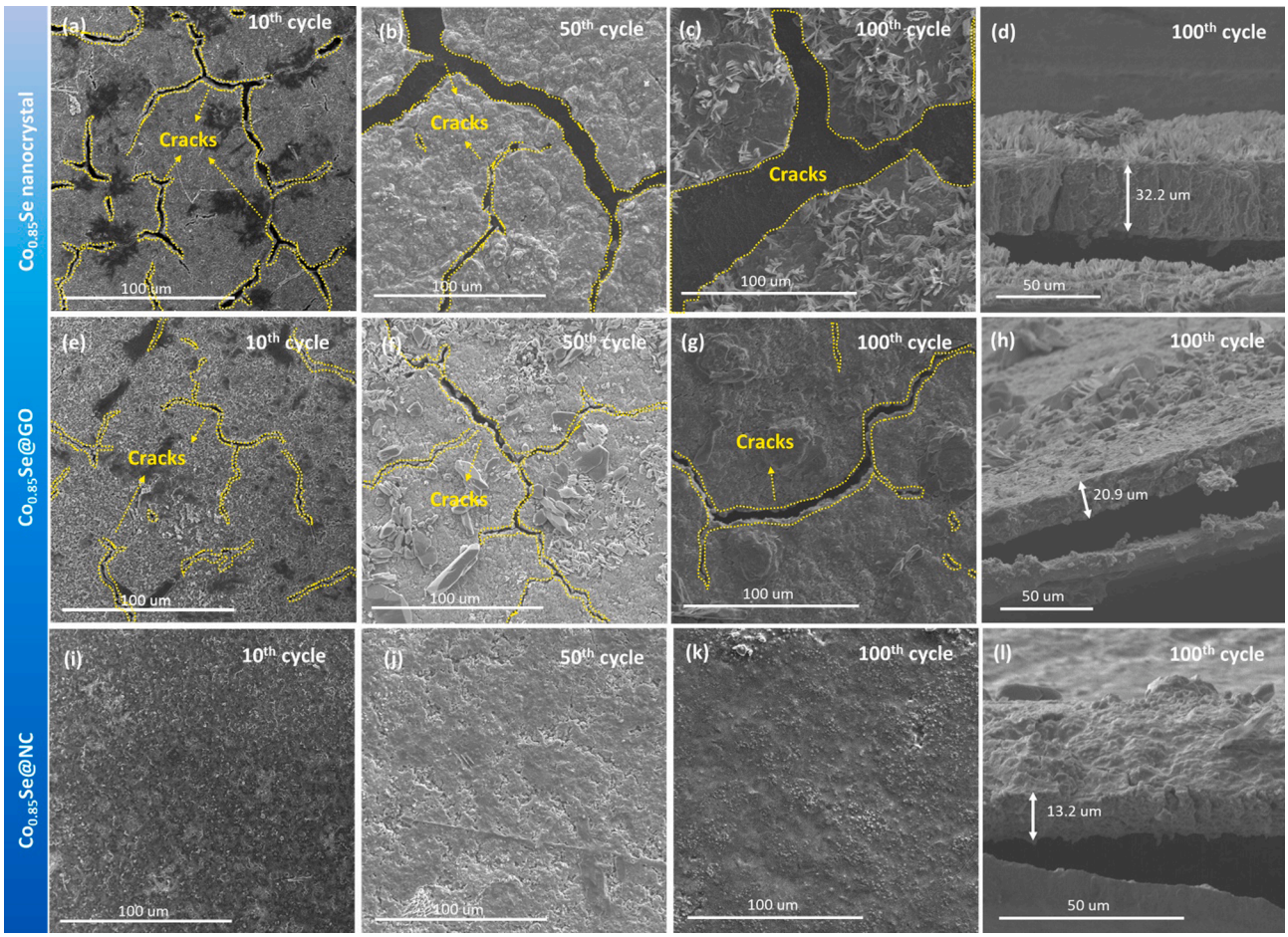

Fig. 6. SEM images of electrode surface. (a-c) $Co_{0.85}Se$ nanocrystal at 10, 50 and 100th cycle. (d) Electrode thickness of $Co_{0.85}Se$ nanocrystal at 100th cycle. (e-g) $Co_{0.85}Se$@GO at 10, 50 and 100th cycle. (h) Electrode thickness of $Co_{0.85}Se$@GO at 100th cycle. (i-k) $Co_{0.85}Se$@NC at 10, 50 and 100th cycle. (l) Electrode thickness of $Co_{0.85}Se$@NC at 100th cycle.

17.59, and 7.18 mA h g^{-1} (Fig. 7f), the capacity retentions (relative to 1.75 mg cm^{-2}) were 45.2, 27.9, 16.8, 8.4, 4.0%, respectively (Fig. 7i). In summary, only $Co_{0.85}Se$@NC maintains more than 65% in capacity retention with increasing current density. Without stress management, $Co_{0.85}Se$@NC and $Co_{0.85}Se$ nanocrystal have the largest capacity difference between 197.9 and 135.63 mA h g^{-1} at 100 and 2500 mA g^{-1}, respectively. As for 3D and 2D carbonaceous compounds, the differences between them are 50.13 and 82.17 mA h g^{-1}, respectively. All the above results indicate that the 3D carbon matrix is the greatest management for stress relaxation. Fig. 7i is a comparison diagram of the charge transfer impedance of the three half-cells with a loading mass of 3.8 mg cm^{-2}. The volume expansion during cycling is more apparent in the high-loading mass half-cell. Although the activation of the electrode after cycling can lower the charge transfer resistance. However, through the control of stress, the $Co_{0.85}Se$@NC of the three-dimensional carbon framework can have the best performance. The slope obtained from the linear plot of Re(Z) and $\omega^{-1/2}$ is the Warburg factor. Fig. 7j is the Warburg factor statistics before and after the cycle. $Co_{0.85}Se$@NC has a larger value before cycling (Fig. S13a, b) is attributed to the difficulty of potassium ion diffusion in the three-dimensional carbon framework compared with the others.[54] After the cycling test, only $Co_{0.85}Se$@NC greatly reduces the value, and the rest are increased due to the high loading mass. The diffusion coefficient of K^+ can be further calculated by Eq. (3) in the generality and low-frequency range of diffusion.

$$D_{K+} = \frac{0.5R^2T^2}{A^2n^4F^4C^2\sigma^2} \quad (3)$$

After cycling, the diffusion coefficient of $Co_{0.85}Se$@NC is increased by 2816%, while that of $Co_{0.85}Se$ nanocrystals and $Co_{0.85}Se$@GO is decreased by 81% and 89%, respectively, confirming the advantages of stress regulation. We have also conducted long-term cycling tests of the high-loading mass electrode (Fig. 7m), the 3D structure can provide at least 200 cycles and maintain a relatively high specific capacity of 458.5 mA h g^{-1} at 500 mA g^{-1}. Further, we also push the areal capacity up to 1.03 mA h cm^{-2} for at least 100 cycles (Fig. 7n). The $Co_{0.85}Se$@NC with an excellent performance among anodes in the PIBs field as shown in Fig. 7o [61–65].

Based on the excellent electrochemical performance of $Co_{0.85}Se$@NC in the half-cell, we further assembled a potassium-ion full battery. The Prussian blue (PB) is used as the cathode material, and it is the common name for the chemical compound, iron (III) hexacyanoferrate (II), $Fe_4^{III}[Fe^{II}(CN)_6]_3$. PB can reversibly intercalate K ions for long-term cycling tests without affecting the crystal structure and thus minimized the capacity fade [66]. Due to the high oxidation potential of the conversion K_2Se, organic cathodes such as PTCDA cannot meet a high working plateau over 3.5 V [67,68]. Prussian blue analogs can both cover the working range of the anodic conversion reaction and maintain decent cycling performance. The schematic diagram of the potassium ion full battery system is shown in Fig. 8a. The PB in a stable spinel structure was synthesized by the precipitation method, which can stably receive the diffused potassium ions from the negative electrode. The corresponding XRD pattern and electrochemical performances of PB are shown in Fig. S15. From the CV curve with a scan rate of 1 mV s^{-1} (Fig. 8b), the overlapped peaks revealed the high reversibility of the

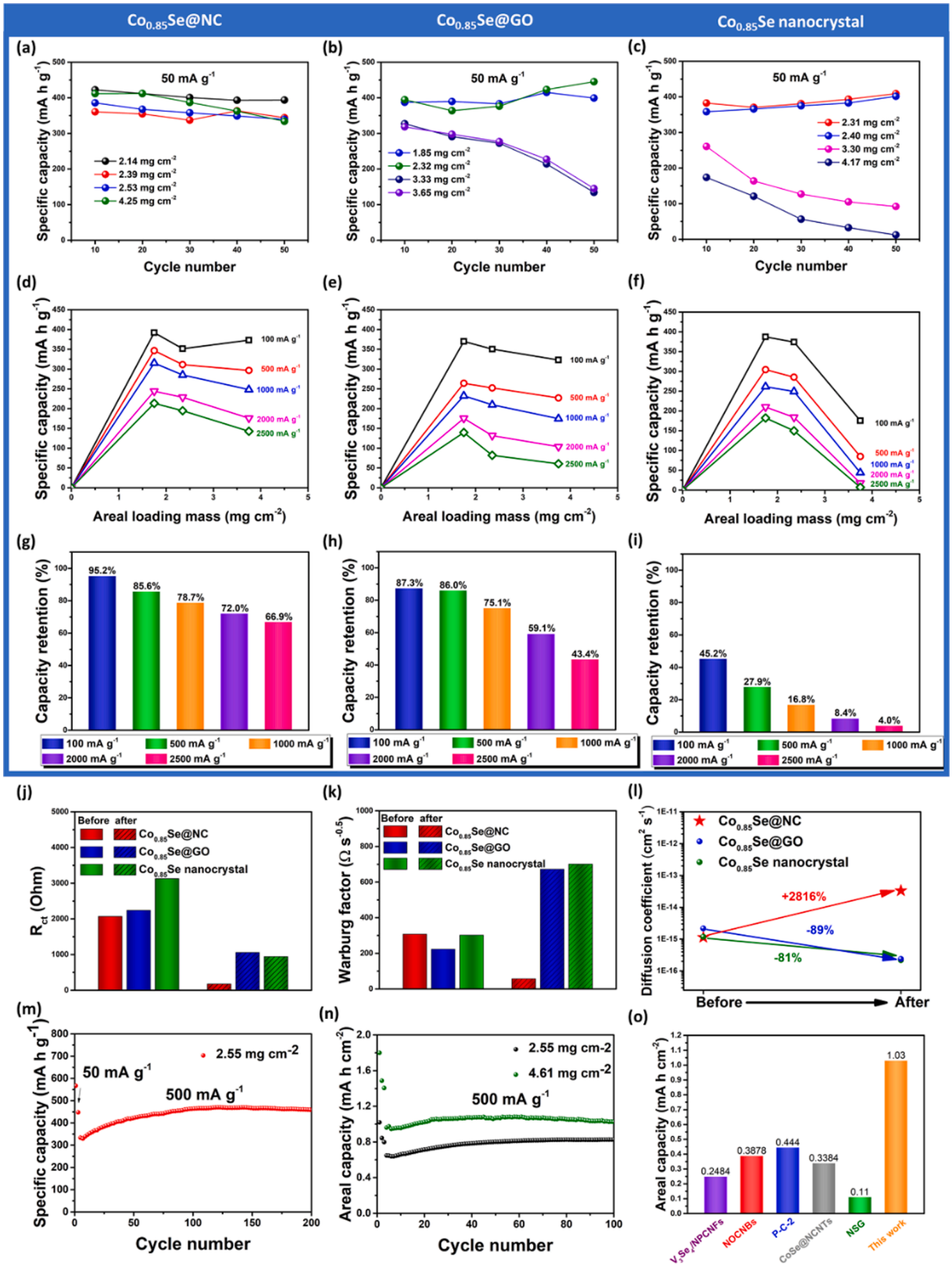

Fig. 7. Different loading mass of (a) $Co_{0.85}Se$@NC, (b) $Co_{0.85}Se$@GO and (c) $Co_{0.85}Se$ nanocrystal at 50 mA g^{-1}. Rate performance of different loading mass for (d) $Co_{0.85}Se$@NC, (e) $Co_{0.85}Se$@GO and (f) $Co_{0.85}Se$ nanocrystal at 0.1, 0.5, 1, 2 and 2.5 A g^{-1}. Corresponding Capacity retention of (g) $Co_{0.85}Se$@NC, (h) $Co_{0.85}Se$@GO and (i) $Co_{0.85}Se$ nanocrystal from 1.75 to 3.75 mg cm^{-2}. (j) Charge transfer resistance comparison. (k) Corresponding Warburg factor comparison. (l) K^+ diffusion coefficient calculated from (k). (m-n) Cycling performance of different loading mass electrode. (o) Areal capacity comparison of anode in PIBs.

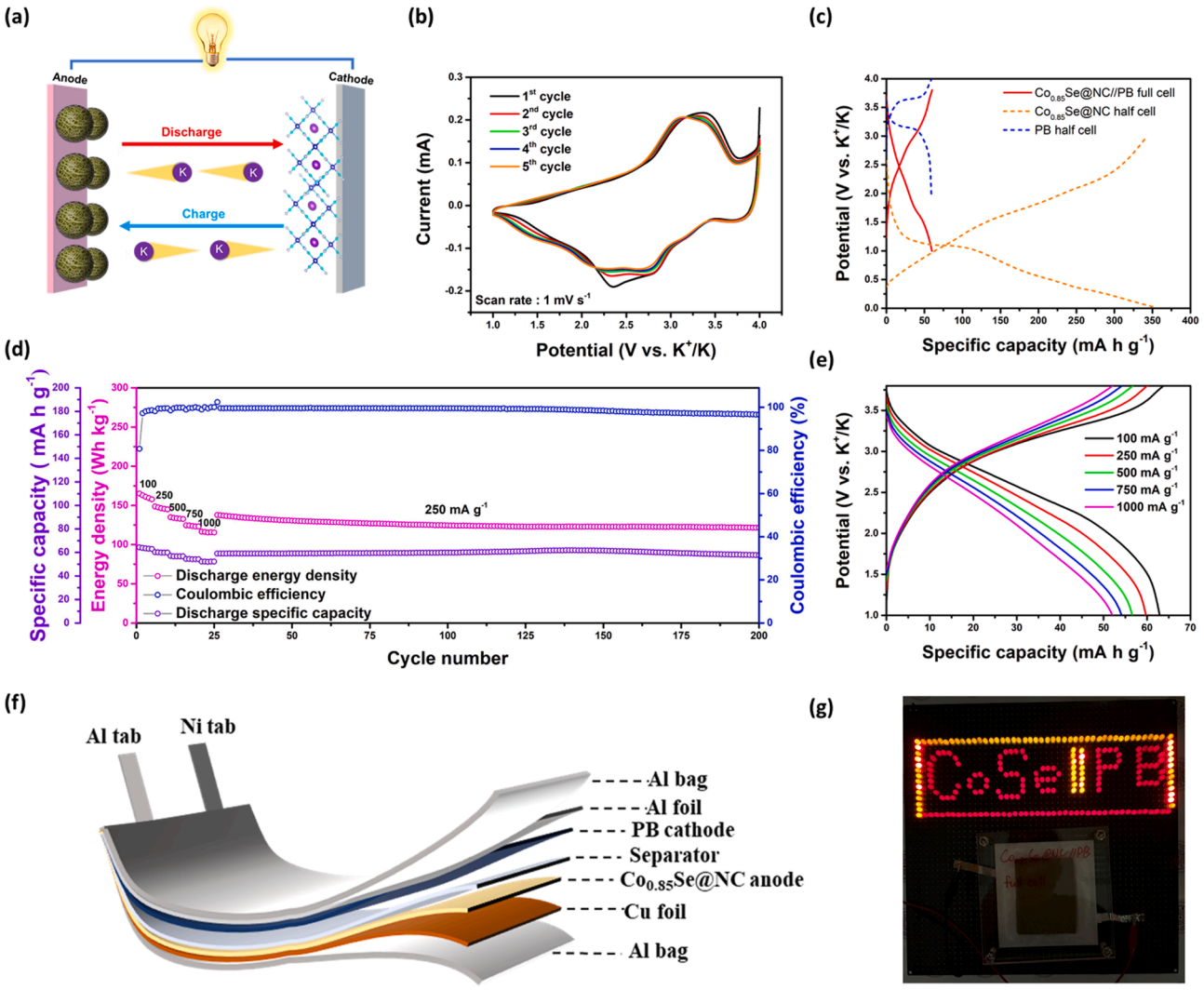

Fig. 8. Potassium ion battery full cell test. (a) Schematic illustration of $Co_{0.85}Se$@NC//PB full cell. (b) CV profiles at a scan rate of 1 mV s^{-1}. (c) $Co_{0.85}Se$@NC half cell, PB half cell, and $Co_{0.85}Se$@NC//PB full cell GCD profiles. (d) Long-term cycling performance at 250 mA g^{-1}. (e) Corresponding GCD profiles at various current density. (f) Schematic illustration of pouch type full cell. (g) Lighting test of $Co_{0.85}Se$@NC//PB pouch type full cell.

chemical reaction and the $Co_{0.85}Se$@NC//PB full cell is in the proper voltage window of 1.0–3.8 V. The charge–discharge curves of $Co_{0.85}Se$@NC half-cell, PB half-cell, and $Co_{0.85}Se$@NC//PB full-cell at 250 mA g^{-1} are shown in Fig. 8c. In addition, we also measured $Co_{0.85}Se$@NC//PB full cell (Fig. 8d-e), which provided average discharge energy densities of 161, 146.5, 133.5, 123.7, 115.4 Wh kg^{-1} at 100, 250, 500, 750, 1000 mA g^{-1}. The capacity loss in each interval is about 6%. After the current density is returned to 250 mA g^{-1}, it still maintains excellent stability. The Coulombic efficiency is still maintained at 96.6% at 200th cyclewith a specific capacity of 121.57 Wh kg^{-1}. In order to determine its practicality, we successfully lighten up 223 LED bulbs by assembling a pouch-type potassium-ion full battery (Fig. 8f-g).

3. Conclusion

This work fully demonstrates the importance of the design strategy between metal chalcogenides and carbonaceous materials, which makes $Co_{0.85}Se$@NC has the characteristics of small crystal size and stress regulation to be stable in the electrochemical test. The finite element analysis simulation has predicted that this structure has the most excellent function of dispersing stress. In electrochemical performance, $Co_{0.85}Se$@NC provides ultra-stable cycling performance and high-rate charge–discharge capability; the porous structure brings high specific surface area and fast reaction kinetics. At the same time, we also revealed the structural changes of during the cycling process. At the micro level, the 3D structure solves the nanoparticles' aggregation and offers a fast ion diffusion path. In the view of the macro level, changes of cracks on the electrode surface after cycling also provide the importance of stress control. Since there are few studies detailing the stress management strategies in potassium ion storage systems, we successfully revealed the dependence of stress management between electrochemical performance and the electrode's loading mass by a serial electrochemical test. Moreover, we successfully lit up two hundred LED bulbs by assembling a pouch-type full battery. This work provides a reliable stress-management strategy for future anode materials and also raises the practical properties of potassium ion batteries to another level.

4. Experimental section

4.1. Materials

Cobalt(II) nitrate hexahydrate (ACS, 98.0 ~ 102.0%), Glycerol (anhydrous, 99), Selenium powder (~325 mesh, 99.5%, metal basis), Sodium selenite (44–46% Se anhydrous), Sodium borohydride (powder, ≧98.0%), GO solution (1 wt%, ≧98%), sodium carboxymethyl cellulose

(NaCMC, average $M_w \sim 700{,}000$), dimethyl ether (DME, ≧99.8%), potassium metal (chunks in mineral oil, 98%), $FeCl_2{\cdot}4H_2O$ (98%), $K_4Fe(CN)_6{\cdot}3H_2O$ (99.5%), potassium citrate (99–100.5%), and Potassium chloride (99%) were purchased from Sigma-Aldrich. Potassium bis(fluorosulfonyl)imide (KFSI, 97%) was purchased from Combi-Blocks. Super-P, polyvinylidene fluoride (PVDF) and coin-type cell CR2032 were purchased from shining energy. Glass fiber was purchased from Advantec. Copper and aluminum foil were purchased from Chang-Chun group.

4.2. Material characterization

The crystal purity was determined by an X-ray diffractometer (XRD, Bruker D8 ADVANCE) with a Cu-Kα source (λ = 1.54056 Å). The morphologies of the obtained samples were examined by employing scanning electron microscopy (SEM, HITACHI-SU8010) and an energy dispersive spectrometer (EDS) was used for elemental mapping. Transmission electron microscopy (TEM, JEOL, JEM-ARM200FTH, serviced provided by NTHU and NYCU) with an accelerating voltage of 200 kV for investigating structural analysis including morphology, crystal d-spacing, and selected-area electron diffraction (SAED). The chemical state was examined by high-resolution X-ray photoelectron spectroscopy (XPS, ULVAC-PH, PHI QuanteraII). All the spectra obtained from the XPS analysis were first calibrated by referencing the standard binding energy of C 1s (284.8 eV). Raman spectrum was measured via a LABRAM HR 800 UV with a 532 nm excitation source. TGA analysis was obtained using a thermogravimetric analyzer (TA, Q50) in an air flow at a heating rate of 10 °C min^{-1} from ambient temperature to 800 °C.

4.3. Synthesis of Co-glycerate

Co-glycerate was synthesized via a simple solvothermal. First, 1 mmol of $Co(NO_3)_2{\cdot}6H_2O$ was dissolved into 52.5 mL of IPA and stirred (500 rpm) for 30 min. Then 7.5 mL glycerol and 1 mL DI water were slowly dropped into the above solution and stirred (500 rpm) for 15 min. During the whole process, the temperature was kept between 8 ~ 12 °C. The above solution was then transferred into a 100 mL Teflon-lined stainless autoclave maintained at 190 °C for 12 h.

4.4. Synthesis of Co-glycerate@PDA

Co-glycerate@PDA was synthesized by adding 100 mg of Co-glycerate and 50 mg of dopamine hydrochloride into 0.01 M, 100 mL Tris-buffer solution, then sonication for 1 min before stirring (500 rpm) for 4 h. The products were collected by centrifugation (10 min per cycle at 10000 rpm) three times using Ethanol and DI water.

4.5. Synthesis of $Co_{0.85}Se$@NC

Firstly, Co-glycerate@PDA (130 mg) and Se powder (780 mg) were put into a quartz boat and annealed under Ar/H_2 atmosphere for 7.5 h (3 °C min^{-1}) to obtain $Co_{0.85}Se$@NC.

4.6. Synthesis of $Co_{0.85}Se$ nanocrystal

Firstly, 0.546 g of cobalt chloride and 0.726 g of sodium selenite, and 0.5 g of sodium borohydride were dissolved in 40 mL of DI water, followed by 10 min stirring. Then transferred into a 50 mL Teflon-lined stainless autoclave maintained at 180 °C for 24 h [69].

4.7. Synthesis of $Co_{0.85}Se$@GO

Firstly, 0.546 g of cobalt chloride and 0.726 g of sodium selenite, and 0.5 g of sodium borohydride were dissolved in a solution with 25 mL DI water and 15 mL GO solution, followed by 10 min stirring. Then transferred into a 50 mL Teflon-lined stainless autoclave maintaining at 180 °C for 24 h.

4.8. Synthesis of PB cathode

Firstly, solution A was prepared by dissolving 3 mmol of $FeCl_2{\cdot}4H_2O$ in 100 mL of DI water, while solution B was prepared by dissolving 5 mmol of $K_4Fe(CN)_6{\cdot}3H_2O$, 10 mmol of potassium citrate, and 12 g of potassium chloride in 100 mL of DI water. Then, Solution B was slowly added to solution A with a dripping rate of 50 mL hr^{-1} under 400 rpm stirring for 4 h. The precipitates were collected by centrifugation and washed with the mixture of ethanol and DI water for 3 times, and finally dried in a vacuum oven for 2 h at 80 °C.

4.9. Electrochemical measurement

The electrochemical performances of the electrodes were evaluated using CR2032 coin-type cells. A homogeneous slurry of anode material was prepared by mixing 70 wt% of active material, 20 wt% of NaCMC, and 10 wt% of SuperP in Deionized water. The mixture was coated on copper foil and then dried at 80 °C under Argon atmosphere. The average mass loading for the half cell was about 0.8 ~ 1.0 mg cm^{-2}. K metal and glass fiber were used as counter electrode and separator, respectively. The electrolyte used in the cell was 4 M KFSI in DME (~160 μL per cell). For full cell assembly, PB was used as cathode material, and prepotassiated for 20 cycles at 250 mA g^{-1}, while the anode material was also prepotassiated for 20 cycles at 500 mA g^{-1}. The mass ratio of cathode to anode were 4.5/1. The whole assembly process was performed in an Argon-filled glove box. The cyclic voltammetry (CV) and electrochemical impedance spectroscopy (EIS) tests were collected by a multi-channel electrochemical analyzer (Bio-Logic-science Instruments, VMP3). The electrochemical performances were tested on Neware battery analyzer (Neware, China) in the potential range of 0.01–3 V (vs. K^+/K). The galvanostatic intermittent titration technique (GITT) was evaluated by Maccor Series 4000 battery test system.

4.10. Finite element analysis simulation

A perfectly elastic–plastic model was used to describe the potassiation-induced deformation, and a nonlinear diffusion model was used to simulate the particle diffusion process. The simulation and pre- and post-processing processes were all carried out in COMSOL 6.1. Since the governing equations of thermal diffusion and mass diffusion are the same, the diffusion and stress–strain fields in COMSOL were replaced by the temperature-displacement coupling program. The thermal expansion coefficient was used instead of the potassiation expansion coefficient βij, and the temperature field was substituted for the normalized K^+ concentration c. In the model, it was assumed that the volume of cobalt selenide increases by 312% after complete diffusion, the volume expansion coefficient of cobalt selenide was set at $\beta_{ij} = 1.49*10^{-5}$ [70], and the volumes of graphene and amorphous carbon remain unchanged. Under ideal conditions, graphene and amorphous carbon as the outer boundary, with uniform Co and K_2Se and constant elastic modulus and Poisson's ratio, which provide support for the mechanical confinement of $Co_{0.85}Se$.

CRediT authorship contribution statement

Wei-Wen Shen: Conceptualization, Methodology, Data curation. **Yi-Yen Hsieh:** Methodology, Data curation. **Hsing-Yu Tuan:** Conceptualization, Resources, Supervision, Writing – review & editing.

Declaration of Competing Interest

The authors declare that they have no known competing financial interests or personal relationships that could have appeared to influence the work reported in this paper.

Data availability

No data was used for the research described in the article.

Acknowledgments

This work received financial support from the 2030 Cross-Generation Young Scholars Program by National Science and Technology Council, Taiwan (NSTC 112-2628-E-007-010). H.-Y. Tuan also acknowledges the financial support of National Tsing Hua University, Taiwan, through Grant No. 109QI030E1.The authors thank the technical support from Ms. Y. M. Chang in Instrumentation Center at National Tsing Hua University.

Appendix A. Supplementary data

Supplementary data to this article can be found online at https://doi.org/10.1016/j.jcis.2023.04.018.

References

[1] M. Fichtner, K. Edström, E. Ayerbe, M. Berecibar, A. Bhowmik, I.E. Castelli, S. Clark, R. Dominko, M. Erakca, A.A. Franco, Rechargeable batteries of the future—the state of the art from a BATTERY 2030+ perspective, Adv. Energy Mater. 12 (17) (2022) 2102904, https://doi.org/10.1002/aenm.202102904.
[2] R. Schlögl, Chemical energy storage enables the transformation of fossil energy systems to sustainability, Green Chem. 23 (4) (2021) 1584–1593, https://doi.org/10.1039/D0GC03171B.
[3] Z. Yang, H. Huang, F. Lin, Sustainable Electric Vehicle Batteries for a Sustainable World: Perspectives on Battery Cathodes, Environment, Supply Chain, Manufacturing, Life Cycle, and Policy, Adv. Energy Mater. 2200383 (2022), https://doi.org/10.1002/aenm.202200383.
[4] J. Ma, Y. Li, N.S. Grundish, J.B. Goodenough, Y. Chen, L. Guo, Z. Peng, X. Qi, F. Yang, L. Qie, The 2021 battery technology roadmap, J. Phys. D 54 (18) (2021) 183001, https://doi.org/10.1088/1361-6463/abd353.
[5] A. Eftekhari, Potassium secondary cell based on Prussian blue cathode, J. Power Sources 126 (1–2) (2004) 221–228, https://doi.org/10.1016/j.jpowsour.2003.08.007.
[6] A. Eftekhari, Z. Jian, X. Ji, Potassium secondary batteries, ACS Appl. Mater. Inter. 9 (5) (2017) 4404–4419, https://doi.org/10.1021/acsami.6b07989.
[7] J. Mao, C. Wang, Y. Lyu, R. Zhang, Y. Wang, S. Liu, Z. Wang, S. Zhang, Z. Guo, Organic electrolyte design for practical potassium-ion batteries, J. Mater. Chem. A (2022), https://doi.org/10.1039/D2TA02223K.
[8] S. Liu, J. Mao, L. Zhang, W.K. Pang, A. Du, Z. Guo, Manipulating the solvation structure of nonflammable electrolyte and Interface to enable unprecedented stability of graphite anodes beyond 2 years for safe potassium-ion batteries, Adv. Mater. 33 (1) (2021) 2006313, https://doi.org/10.1002/adma.202006313.
[9] Z. Jian, W. Luo, X. Ji, Carbon electrodes for K-ion batteries, J. Am. Chem. Soc. 137 (36) (2015) 11566–11569, https://doi.org/10.1021/jacs.5b06809.
[10] C.B. Chang, H.Y. Tuan, Recent Progress on Sb-and Bi-based Chalcogenide Anodes for Potassium-Ion Batteries, Chem. Asian J. (2022) e202200170.
[11] C.-B. Chang, K.-T. Chen, H.-Y. Tuan, Large-scale synthesis of few-layered copper antimony sulfide nanosheets as electrode materials for high-rate potassium-ion storage, J. Colloid Interface Sci. 608 (2022) 984–994, https://doi.org/10.1016/j.jcis.2021.09.154.
[12] W. Feng, H. Wang, Y. Jiang, H. Zhang, W. Luo, W. Chen, C. Shen, C. Wang, J. Wu, L. Mai, A Strain-Relaxation Red Phosphorus Freestanding Anode for Non-Aqueous Potassium Ion Batteries, Adv. Energy Mater. 12 (7) (2022) 2103343, https://doi.org/10.1002/aenm.202103343.
[13] F.-W. Yuan, H.-J. Yang, H.-Y. Tuan, Seeded silicon nanowire growth catalyzed by commercially available bulk metals: broad selection of metal catalysts, superior field emission performance, and versatile nanowire/metal architectures, J. Mater. Chem. 21 (36) (2011) 13793–13800, https://doi.org/10.1039/C1JM11956G.
[14] J. Wu, S. Liu, Y. Rehman, T. Huang, J. Zhao, Q. Gu, J. Mao, Z. Guo, Phase Engineering of Nickel Sulfides to Boost Sodium-and Potassium-Ion Storage Performance, Adv. Funct. Mater. 31 (27) (2021) 2010832, https://doi.org/10.1002/adfm.202010832.
[15] Y. Wu, C. Zhang, H. Zhao, Y. Lei, Recent advances in ferromagnetic metal sulfides and selenides as anodes for sodium-and potassium-ion batteries, J. Mater. Chem. A 9 (15) (2021) 9506–9534, https://doi.org/10.1039/D1TA00831E.
[16] J. Ge, B. Wang, J. Wang, Q. Zhang, B. Lu, Nature of FeSe2/N-C anode for high performance potassium ion hybrid capacitor, Adv. Energy Mater. 10 (4) (2020) 1903277, https://doi.org/10.1002/aenm.201903277.
[17] W. Zhang, Y. Liu, Z. Guo, Approaching high-performance potassium-ion batteries via advanced design strategies and engineering, Sci. Adv. 5 (5) (2019) eaav7412, https://doi.org/10.1126/sciadv.aav7412.
[18] Y. Zhao, L.P. Wang, M.T. Sougrati, Z. Feng, Y. Leconte, A. Fisher, M. Srinivasan, Z. Xu, A review on design strategies for carbon based metal oxides and sulfides nanocomposites for high performance Li and Na ion battery anodes, Adv. Energy Mater. 7 (9) (2017) 1601424, https://doi.org/10.1002/aenm.201601424.
[19] Y.-F. Huang, Y.-C. Yang, Y.-Y. Tseng, H.-Y. Tuan, Two dimensional MnPSe3 layer stacking composites with superior storage performance for alkali metal-ion batteries, J. Colloid Interface Sci. 635 (2023) 336–347, https://doi.org/10.1016/j.jcis.2022.12.082.
[20] Z. Wang, K. Dong, D. Wang, S. Luo, X. Liu, Y. Liu, Q. Wang, Y. Zhang, A. Hao, C. He, Constructing N-Doped porous carbon confined FeSb alloy nanocomposite with Fe-NC coordination as a universal anode for advanced Na/K-ion batteries, Chem. Eng. J. 384 (2020) 123327, https://doi.org/10.1016/j.cej.2019.123327.
[21] Z. Shadike, M.-H. Cao, F. Ding, L. Sang, Z.-W. Fu, Improved electrochemical performance of CoS 2–MWCNT nanocomposites for sodium-ion batteries, Chem comm 51 (52) (2015) 10486–10489, https://doi.org/10.1039/C5CC02564H.
[22] Y.-F. Huang, Y.-C. Yang, H.-Y. Tuan, Construction of strongly coupled few-layer FePSe3-CNT hybrids for high performance potassium-ion storage devices, Chem. Eng. J. 451 (2023), 139013, https://doi.org/10.1016/j.cej.2022.139013.
[23] Y.-Y. Hsieh, H.-Y. Tuan, Architectural van der Waals Bi2S3/Bi2Se3 topological heterostructure as a superior potassium-ion storage material, Energy Storage Mater. 51 (2022) 789–805, https://doi.org/10.1016/j.ensm.2022.07.020.
[24] S.-F. Ho, H.-Y. Tuan, Cu3PS4: a sulfur-rich metal phosphosulfide with superior ionic diffusion channel for high-performance potassium ion batteries/hybrid capacitors, Chem. Eng. J. 452 (2023) 139199, https://doi.org/10.1016/j.cej.2022.139199.
[25] Y. Zhao, J. Zhu, S.J.H. Ong, Q. Yao, X. Shi, K. Hou, Z.J. Xu, L. Guan, High-rate and ultralong cycle-life potassium ion batteries Enabled by in situ engineering of yolk–shell FeS2@ C structure on graphene matrix, Adv. Energy Mater. 8 (36) (2018) 1802565, https://doi.org/10.1002/aenm.201802565.
[26] K.-T. Chen, S. Chong, L. Yuan, Y.-C. Yang, H.-Y. Tuan, Conversion-alloying dual mechanism anode: Nitrogen-doped carbon-coated Bi2Se3 wrapped with graphene for superior potassium-ion storage, Energy Storage Mater. 39 (2021) 239–249, https://doi.org/10.1016/j.ensm.2021.04.019.
[27] H. Gao, T. Zhou, Y. Zheng, Q. Zhang, Y. Liu, J. Chen, H. Liu, Z. Guo, CoS quantum dot nanoclusters for high-energy potassium-ion batteries, Adv. Funct. Mater. 27 (43) (2017) 1702634, https://doi.org/10.1002/adfm.201702634.
[28] L. Wu, J. Lang, P. Zhang, X. Zhang, R. Guo, X. Yan, Mesoporous Ni-doped MnCo 2 O 4 hollow nanotubes as an anode material for sodium ion batteries with ultralong life and pseudocapacitive mechanism, J. Mater. Chem. A 4 (47) (2016) 18392–18400, https://doi.org/10.1039/C6TA08364A.
[29] X. Gao, P. He, J. Ren, J. Xu, Modeling of contact stress among compound particles in high energy lithium-ion battery, Energy Storage Mater. 18 (2019) 23–33, https://doi.org/10.1016/j.ensm.2019.02.007.
[30] X. Zhang, Y. Zhou, B. Luo, H. Zhu, W. Chu, K. Huang, Microwave-assisted synthesis of NiCo2O4 double-shelled hollow spheres for high-performance sodium ion batteries, Nanomicro Lett 10 (1) (2018) 1–7, https://doi.org/10.1007/s40820-017-0164-2.
[31] M. Ji, N. Jiang, J. Chang, J. Sun, Near-infrared light-driven, highly efficient bilayer actuators based on polydopamine-modified reduced graphene oxide, Adv. Funct. Mater. 24 (34) (2014) 5412–5419, https://doi.org/10.1002/adfm.201401011.
[32] S.-C. Lu, M.-C. Hsiao, M. Yorulmaz, L.-Y. Wang, P.-Y. Yang, S. Link, W.-S. Chang, H.-Y. Tuan, Single-crystalline copper nano-octahedra, Chem. Mater. 27 (24) (2015) 8185–8188, https://doi.org/10.1021/acs.chemmater.5b03519.
[33] Y. Feng, M. Xu, T. He, B. Chen, F. Gu, L. Zu, R. Meng, J. Yang, CoPSe: A New Ternary Anode Material for Stable and High-Rate Sodium/Potassium-Ion Batteries, Adv. Mater. 33 (16) (2021) 2007262, https://doi.org/10.1002/adma.202007262.
[34] L. Wang, Q. Jiang, K. Yang, Y. Sun, T. Zhou, Z. Huang, H.-J. Yang, J. Hu, Self-assembly of carbon nanotubes on a hollow carbon polyhedron to enhance the potassium storage cycling stability of metal organic framework-derived metallic selenide anodes, J. Colloid Interface Sci. 601 (2021) 60–69, https://doi.org/10.1016/j.jcis.2021.05.064.
[35] H. Li, Z. Cheng, Q. Zhang, A. Natan, Y. Yang, D. Cao, H. Zhu, Bacterial-derived, compressible, and hierarchical porous carbon for high-performance potassium-ion batteries, Nano Lett. 18 (11) (2018) 7407–7413, https://doi.org/10.1021/acs.nanolett.8b03845.
[36] A. Ferté, J. Palaudoux, F. Penent, H. Iwayama, E. Shigemasa, Y. Hikosaka, K. Soejima, K. Ito, P. Lablanquie, R. Taïeb, Advanced computation method for double core hole spectra: Insight into the nature of intense shake-up satellites, J. Phys. Chem. Lett. 11 (11) (2020) 4359–4366, https://doi.org/10.1021/acs.jpclett.0c01167.
[37] R. Xu, Y. Yao, H. Wang, Y. Yuan, J. Wang, H. Yang, Y. Jiang, P. Shi, X. Wu, Z. Peng, Unraveling the Nature of Excellent Potassium Storage in Small-Molecule Se@ Peapod-Like N-Doped Carbon Nanofibers, Adv. Mater. 32 (52) (2020) 2003879, https://doi.org/10.1002/adma.202003879.
[38] B. Li, Z. He, J. Zhao, W. Liu, Y. Feng, J. Song, Advanced Se3P4@ C anode with exceptional cycling life for high performance potassium-ion batteries, Small 16 (6) (2020) 1906595, https://doi.org/10.1002/smll.201906595.
[39] T. Li, Y. Wang, L. Yuan, Q. Zhou, S. Qiao, Z. Liu, S. Chong, An α-MnSe nanorod as anode for superior potassium-ion storage via synergistic effects of physical encapsulation and chemical bonding, Chem. Eng. J. 137152 (2022), https://doi.org/10.1016/j.cej.2022.137152.
[40] J. Zhou, D. Shen, X. Yu, B. Lu, Building ultra-stable K-Te battery by molecular regulation, J. Energy Chem. 69 (2022) 100–107, https://doi.org/10.1016/j.jechem.2021.10.001.
[41] C. Wu, Y. Lei, L. Simonelli, D. Tonti, A. Black, X. Lu, W.H. Lai, X. Cai, Y.X. Wang, Q. Gu, Continuous Carbon Channels Enable Full Na-Ion Accessibility for Superior Room-Temperature Na–S Batteries, Adv. Mater. 34 (8) (2022) 2108363, https://doi.org/10.1002/adma.202108363.
[42] Y. Jin, L. Dang, H. Zhang, C. Song, Q. Lu, F. Gao, Synthesis of unit-cell-thick α-Fe2O3 nanosheets and their transformation to γ-Fe2O3 nanosheets with

enhanced LIB performances, Chem. Eng. J. 326 (2017) 292–297, https://doi.org/10.1016/j.cej.2017.05.155.
[43] X. Chen, H. Muheiyati, X. Sun, P. Zhou, P. Wang, X. Ding, Y. Qian, L. Xu, Rational Design of Tungsten Selenide@ N-Doped Carbon Nanotube for High-Stable Potassium-Ion Batteries, Small 18 (5) (2022) 2104363, https://doi.org/10.1002/smll.202104363.
[44] X. Chen, M. Li, S.P. Wang, C. Wang, Z. Shen, F.Q. Bai, F. Du, In Situ Fabrication of Cuprous Selenide Electrode via Selenization of Copper Current Collector for High-Efficiency Potassium-Ion and Sodium-Ion Storage, Adv. Sci. 9 (5) (2022) 2104630, https://doi.org/10.1002/advs.202104630.
[45] G. Suo, J. Zhang, D. Li, Q. Yu, W.A. Wang, M. He, L. Feng, X. Hou, Y. Yang, X. Ye, N-doped carbon/ultrathin 2D metallic cobalt selenide core/sheath flexible framework bridged by chemical bonds for high-performance potassium storage, Chem. Eng. J. 388 (2020) 124396, https://doi.org/10.1016/j.cej.2020.124396.
[46] Z. Kong, L. Wang, S. Iqbal, B. Zhang, B. Wang, J. Dou, F. Wang, Y. Qian, M. Zhang, L. Xu, Iron Selenide-Based Heterojunction Construction and Defect Engineering for Fast Potassium/Sodium-Ion Storage, Small 18 (15) (2022) 2107252, https://doi.org/10.1002/smll.202107252.
[47] C. Wang, H. Qin, L. Cao, D. Wang, J. Zhang, B. Zhang, X. Ou, Engineered single-crystal metal-selenide for rapid K-ion diffusion and polyselenide convention, Chem. Eng. J. 427 (2022) 131963, https://doi.org/10.1016/j.cej.2021.131963.
[48] J.H. Na, Y.C. Kang, S.-K. Park, Electrospun MOF-based ZnSe nanocrystals confined in N-doped mesoporous carbon fibers as anode materials for potassium ion batteries with long-term cycling stability, Chem. Eng. J. 425 (2021) 131651, https://doi.org/10.1016/j.cej.2021.131651.
[49] J. Chu, Q. Yu, K. Han, L. Xing, Y. Bao, W.A. Wang, A novel graphene-wrapped corals-like NiSe2 for ultrahigh-capacity potassium ion storage, Carbon 161 (2020) 834–841, https://doi.org/10.1016/j.carbon.2020.02.020.
[50] H. Shan, J. Qin, Y. Ding, H.M.K. Sari, X. Song, W. Liu, Y. Hao, J. Wang, C. Xie, J. Zhang, Controllable heterojunctions with a semicoherent phase boundary boosting the potassium storage of CoSe2/FeSe2, Adv. Mater. 33 (37) (2021) 2102471, https://doi.org/10.1002/adma.202102471.
[51] J. Ruan, J. Zang, J. Hu, R. Che, F. Fang, F. Wang, Y. Song, D. Sun, Respective Roles of Inner and Outer Carbon in Boosting the K+ Storage Performance of Dual-Carbon-Confined ZnSe, Adv. Sci. 9 (5) (2022) 2104822, https://doi.org/10.1002/advs.202104822.
[52] S. Zhao, D. He, T. Wu, L. Wang, H. Yu, Ultrastable Orthorhombic Na2TiSiO5 Anode for Lithium-Ion Battery, Adv. Energy Mater. 12 (6) (2022) 2102709, https://doi.org/10.1002/aenm.202102709.
[53] Y. Liu, K. Cui, Z. Ma, X. Wang, Pseudocapacitance-induced high-rate potassium storage in CoSe@ NrGo hybrid nanosheets for potassium-ion batteries, Energy Fuels 34 (8) (2020) 10196–10202, https://doi.org/10.1021/acs.energyfuels.0c01929.
[54] C.-H. Chang, K.-T. Chen, Y.-Y. Hsieh, C.-B. Chang, H.-Y. Tuan, Crystal facet and architecture engineering of metal oxide nanonetwork anodes for high-performance potassium ion batteries and hybrid capacitors, ACS nano 16 (1) (2022) 1486–1501, https://doi.org/10.1021/acsnano.1c09863.
[55] Y. Mao, Y. Chen, J. Qin, C. Shi, E. Liu, N. Zhao, Capacitance controlled, hierarchical porous 3D ultra-thin carbon networks reinforced prussian blue for high performance Na-ion battery cathode, Nano Energy 58 (2019) 192–201, https://doi.org/10.1016/j.nanoen.2019.01.048.
[56] J. Tu, H. Tong, X. Zeng, S. Chen, C. Wang, W. Zheng, H. Wang, Q. Chen, Modification of Porous N-Doped Carbon with Sulfonic Acid toward High-ICE/Capacity Anode Material for Potassium-Ion Batteries, Adv. Funct. Mater. 32 (34) (2022) 2204991, https://doi.org/10.1002/adfm.202204991.
[57] S. Dong, D. Yu, J. Yang, L. Jiang, J. Wang, L. Cheng, Y. Zhou, H. Yue, H. Wang, L. Guo, Tellurium: A High-Volumetric-Capacity Potassium-Ion Battery Electrode Material, Adv. Mater. 32 (23) (2020) 1908027, https://doi.org/10.1002/adma.201908027.
[58] C.-Y. Tsai, C.-H. Chang, T.-L. Kao, K.-T. Chen, and H.-Y. Tuan, Shape matters: SnP0. 94 teardrop nanorods with boosted performance for potassium ion storage, Chem. Eng. J. 417 (2021) 128552, https://doi.org/10.1016/j.cej.2021.128552.
[59] G.D. Park, Y.C. Kang, Conversion reaction mechanism for yolk-shell-structured iron telluride-C nanospheres and exploration of their electrochemical performance as an anode material for potassium-ion batteries, Small Methods 4 (10) (2020) 2000556, https://doi.org/10.1002/smtd.202000556.
[60] R. Hu, Y. Ouyang, T. Liang, X. Tang, B. Yuan, J. Liu, L. Zhang, L. Yang, M. Zhu, Inhibiting grain coarsening and inducing oxygen vacancies: the roles of Mn in achieving a highly reversible conversion reaction and a long life SnO 2–Mn–graphite ternary anode, Energy Environ. Sci. 10 (9) (2017), https://doi.org/10.1039/C7EE01635B.
[61] L. Xu, W. Guo, L. Zeng, X. Xia, Y. Wang, P. Xiong, Q. Chen, J. Zhang, M. Wei, Q. Qian, V3Se4 embedded within N/P co-doped carbon fibers for sodium/potassium ion batteries, Chem. Eng. J. 419 (2021) 129607, https://doi.org/10.1016/j.cej.2021.129607.
[62] K. Zhang, Q. He, F. Xiong, J. Zhou, Y. Zhao, L. Mai, L. Zhang, Active sites enriched hard carbon porous nanobelts for stable and high-capacity potassium-ion storage, Nano Energy 77 (2020) 105018, https://doi.org/10.1016/j.nanoen.2020.105018.
[63] W. Xiao, X. Li, B. Cao, G. Huang, C. Xie, J. Qin, H. Yang, J. Wang, X. Sun, Constructing high-rate and long-life phosphorus/carbon anodes for potassium-ion batteries through rational nanoconfinement, Nano Energy 83 (2021) 105772, https://doi.org/10.1016/j.nanoen.2021.105772.
[64] Y. Liu, Q. Deng, Y. Li, Y. Li, W. Zhong, J. Hu, X. Ji, C. Yang, Z. Lin, K. Huang, CoSe@ N-doped carbon nanotubes as a potassium-ion battery anode with high initial coulombic efficiency and superior capacity retention, ACS nano 15 (1) (2021) 1121–1132, https://doi.org/10.1021/acsnano.0c08094.
[65] C. Lu, Z. Sun, L. Yu, X. Lian, Y. Yi, J. Li, Z. Liu, S. Dou, J. Sun, Enhanced kinetics harvested in heteroatom dual-doped graphitic hollow architectures toward high rate printable potassium-ion batteries, Adv. Energy Mater. 10 (28) (2020) 2001161, https://doi.org/10.1002/aenm.202001161.
[66] C. Zhang, Y. Xu, M. Zhou, L. Liang, H. Dong, M. Wu, Y. Yang, Y. Lei, Potassium Prussian blue nanoparticles: a low-cost cathode material for potassium-ion batteries, Adv. Funct. Mater. 27 (4) (2017) 1604307, https://doi.org/10.1002/adfm.201604307.
[67] J. Wang, Z. Xu, J.-C. Eloi, M.-M. Titirici, S.J. Eichhorn, Ice-templated, sustainable carbon aerogels with hierarchically tailored channels for sodium-and potassium-ion batteries, Adv. Funct. Mater. 32 (16) (2022) 2110862, https://doi.org/10.1002/adfm.202110862.
[68] Y.-Y. Hsieh, K.-T. Chen, H.-Y. Tuan, A synergetic SnSb-amorphous carbon composites prepared from polyesterification process as an ultrastable potassium-ion battery anode, Chem. Eng. J. 420 (2021) 130451, https://doi.org/10.1016/j.cej.2021.130451.
[69] C. Manjunatha, S. Lakshmikant, L. Shreenivasa, N. Srinivasa, S. Ashoka, B. Shivraj, M. Selvaraj, U. S. Meda, G. S. Babu, and B. G. Pollet, Development of non-stoichiometric hybrid Co3S4/Co0. 85Se nanocomposites for an evaluation of synergistic effect on the OER performance, Surf. Interfaces 25 (2021) 101161, https://doi.org/10.1016/j.surfin.2021.101161.
[70] L.A. Valdez, M.A. Caravaca, R.A. Casali, Ab-initio study of elastic anisotropy, hardness and volumetric thermal expansion coefficient of ZnO, ZnS, ZnSe in wurtzite and zinc blende phases, J. Phys. Chem. Solids 134 (2019) 245–254, https://doi.org/10.1016/j.jpcs.2019.05.019.